ROTOR AERODYNAMIC AND NOISE UNDER INFLUENCE OF ELASTIC BLADE MOTION AND DIFFERENT FUSELAGE MODELING

Jianping Yin*, Berend G. van der Wall+, Gunther A. Wilke*

*Institute of Aerodynamics and Flow Technology, Helicopter

+Institute of Flight Systems, Helicopter

German Aerospace Center (DLR)

Lilienthalplatz 7, 38108 Braunschweig, Germany

ABSTRACT

This paper addresses the influence of the elastic rotor blade deformation and the aerodynamic interference from the fuselage on the rotor aerodynamics as well as rotor noise characteristics. For this purpose, a BO105 Main Rotor (MR)/Tail Rotor (TR)/Fuselage configuration is chosen for the numerical simulations. An unsteady free wake 3-D panel method (UPM) is used to account non-linear effects associated with the mutual interference between MR/TR/Fuselage. DLR's comprehensive isolated rotor code S4 and Airbus Helicopters' (formerly: Eurocopter) rotor code HOST are coupled with UPM to account for the effect of elastic blade deformation. The effect of fuselage is simulated by using two fuselage models in UPM, (1) potential theory in form of a panelised fuselage and (2) an analytic fuselage influence formulation derived from isolated fuselage simulation based on (1). The advantage of (2) is in its computational efficiency. Finally, to evaluate either the elastic blade deformation or the impact of the fuselage on the noise radiation, the sound propagation into the far field is calculated with DLR's FW-H code APSIM, using UPM unsteady blade loads as input. The numerical results indicate that inclusion of the MR elastic blade deformation in the simulation has clearly improved the correlation against the measured data for the three computed flight conditions. In 6° descent flight where the MR is the major source of noise, inclusion of the fuselage in the simulation has caused a reduction of MR Blade Vortex Interaction (BVI) on the advancing side. This is due to the effect of the upwash of the fuselage, which slows down the rotor downwash, slightly increases the miss distance of the tip vortex. In low speed climb and high speed level flight where the TR is the major source of noise, the inclusion of the fuselage increases slightly the TR self BVI as TR BVI on the advancing side passes over the vertical stabilizer and causes increased TR BVI noise.

ABBREVIATIONS

MR	Main Rotor
TR	Tail Rotor
UPM	Unsteady Panel Method
APSIM	DLR FW-H code APSIM
Flower	DLR structured multi-block computational fluid dynamics code
FW-H	Ffowcs-Williams/Hawkings acoustic analogy
S4	DLR comprehensive rotor code
HOST	Airbus Helicopters comprehensive code
BVI	Blade Vortex Interaction
ADV	Advancing side
RET	Retreating side
FUS	Fuselage
rev	Revolution
V_∞	Flight speed
RPM	Rotor rotations per minute
C_T	Thrust coefficient
Mx	Rotor hub roll moment, positive starboard up, Nm
My	Rotor hub pitch moment, positive nose up, Nm
M_h	Hover tip Mach number
α_{eff}	Effective rotor shaft angle of attack, windtunnel corrected
ψ	Azimuth angle
θ	Blade pitch angle
β	Blade flap angle
θ_{FP}	flight path angle (negative value: descent)
$C_N M^2$	Normal force coefficient

1. INTRODUCTION

Both the elastic rotor blade deformation and the aerodynamic interference from fuselage can affect the design of the helicopter as well as the overall helicopter noise. The studies from coupling of computational fluid dynamics (CFD) and comprehensive codes have shown ever improving predictions [1]. But such an approach is still computationally expensive and is inefficient in predicting blade vortex interaction (BVI), which is important in defining BVI noise radiation in descent flight. Therefore, there is still a need for a more efficient code for the purpose of capturing BVI, such as comprehensive codes with either free wake or

prescribe wake [2] or potential panel codes with free wake which are coupled to dynamic code as elastic response of the blade is a key element for good airloads correlation.

In this paper, MR/TR aerodynamic and noise under the influence of elastic blade motion and different fuselage modeling in various flight conditions are studied using the free wake unsteady panel code and FW-H code developed at DLR Institute of Aerodynamics and Flow Technology, Helicopter Division [3][4][5][6]. The present work is an extension of the authors' previous works[6].

A BO105 MR/TR/Fuselage configuration is chosen for the numerical simulations as shown in Figure 1. The numerical simulations are compared with EU HELINOVI[7][8][9] wind tunnel data. The following contents are included in the paper:

1. DLR methodologies applied in numerical simulation will be described, including the description of the coupling approach;
2. The elastic blade deformation on MR BVI and MR/TR aerodynamics (unsteady blade loads, wake development) as well as the radiated noise will be discussed and compared with HELINOVI wind tunnel data. The flight conditions simulated are descent, climb and level flight at advance ratios of $\mu = 0.151$ and $\mu = 0.275$ respectively.
3. An analytic fuselage influence formulation derived from isolated fuselage simulation is introduced. The effects of different fuselage models are compared and discussed.

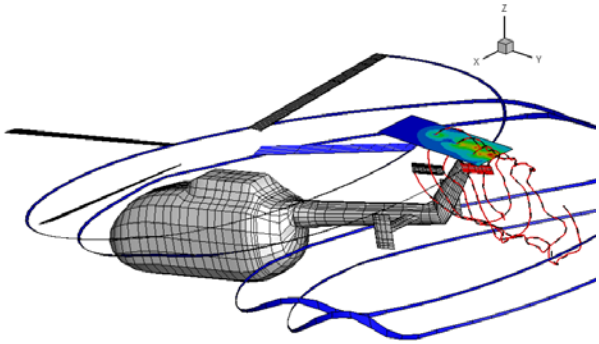

Figure 1 BO105 MR/TR/Fuselage configuration chosen in the numerical simulations

2. DESCRIPTION OF METHODOLOGIES APPLIED IN NUMERICAL SIMULATIONS

The numerical methodology starts with a weak coupling of the unsteady free wake 3-D panel code UPM[4][5][6] and Airbus Helicopters HOST[10] or DLR's comprehensive rotor code S4[2] for computing the trim and deformation of a flexible rotor. For validation purpose, the coupling of DLR CFD Code FLOWer[11] and HOST is also conducted. To evaluate the impact of the blade deformation and the fuselage on the noise radiation, the Ffowcs Williams-Hawkings code APSIM is then applied. The acoustic scattering of the fuselage is not accounted for, yet and will be part of the future research.

2.1 Aerodynamic Model

The 3D unsteady free wake panel code, UPM is used. UPM is a velocity-based, indirect potential formulation – a combination of source and dipole distribution on the solid surfaces and dipole panels in the wake.

2.1.1 Modelling of a lifting rotor blade or a wing

The model of the lifting rotor blade or wing consists of the following elements (Figure 2):

a) A source/sink distribution over the blade surface to simulate the displacement effect of blades with finite thickness.

b) A prescribed weighting function for the vortex strength over the blade or wing chord to account for the blade lift.

c) A short zero-thickness elongation of the trailing edge along its bisector (Kutta panel) to satisfy the Kutta condition. The satisfaction of the flow tangency condition on the Kutta panel fixes the total strength of the circulation in the blade section; its variation over the blade chord is given by b) above. The orientation of the Kutta panel determines the direction of the emission of a wake element at the time of its release from the blade trailing edge.

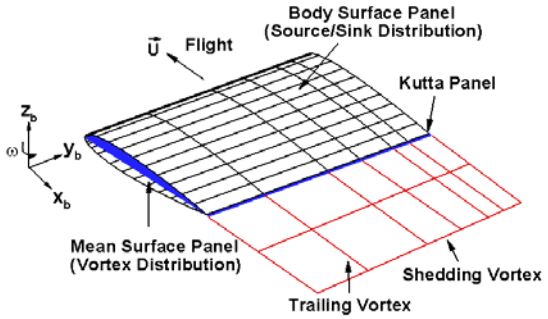

Figure 2 Numerical model of a Blade and Wake

The advantage of the Kutta condition application described in c) is that the additional equations expressing the Kutta condition are linear. It was observed that the numerical Kutta condition without

ensuring pressure equality at the trailing edge was insufficient. An iterative scheme is implemented in order to modify the solution and ensure pressure equality at the trailing edge. This method is proved to be computationally efficient and robust with respect to the size of the chosen time step and the number of panels on the blade.

The pressure on the blade surface is calculated from the unsteady Bernoulli equation. The non-linearity of the problem stems from the a priori unknown spatial location of the wakes. An additional complexity in the case of MR/TR operation arises due to the relative motion between the MR and TR blades, whose consideration is essential to correctly capture the interaction effects.

2.1.2 Modelling of the compressibility effect

The compressibility effect is only considered in computing the normal force coefficient by applying Prandtl-Glauert correction. This is to apply a term of $1/\sqrt{1-M_r^2}$ for each radial position r, where $M_r = V(r)/c_\infty$, $V(r)$ is overall inflow velocity at each radial position and C_∞ is speed of the sound.

2.1.3 Modeling of fuselage

In the current implementation, the fuselage, tail boom and empennage are not considered as a lifting surface and thus contribute zero net vorticity to the flow. To model the presence of a fuselage, two fuselage models are tested,

(1) **Potential theory in form of a panelised fuselage**.

In this model, the fuselage surface is discretized into a system of N quadrilateral panels, as shown in Figure 3. Each panel is represented as a source/sink of constant strength. The velocity at any panel centroid is then given by the sum of the influences from the rotors, fuselage and wakes on the body together with the free stream component of velocity. A boundary condition of zero penetration is enforced simultaneously at the centroids of all panels.

(2) **The Analytic Fuselage Influence Formulation**

The details of the analytic fuselage influence formulation is descripted in [12][13]. The analytical model of the fuselage-induced inflow ratio (referenced to flight speed) applied in the simulation has the following form:

$$\frac{v_i(x,y,z)}{V_\infty} = \frac{A_0 S_A(z)}{S_x(z)(x-x_0)^2/R^2 + S_y(z)(y-y_0)^2/R^2 + 1}$$

$$S_A(z) = \frac{1}{S_{A0}(z-z_0)^2/R^2 + 1}$$

$$S_x(z) = \frac{S_{x0}}{(z-z_0)^2/R^2} \qquad S_y(z) = \frac{S_{y0}}{(z-z_0)^2/R^2}$$

This generic function describes each of the individual upwash and downwash shapes as function of x, y and z. The (x_0,y_0,z_0) is the position of maximum induced velocities. The $S_A(z)$, $S_x(z)$ and $S_y(z)$ are called shape functions. For example, the function $S_A(z)$ has the form of a bell curve and the parameter S_{A0} therein defines its shape. The A_0, S_{x0} and S_{y0} are the peak values for the above mentioned functions.

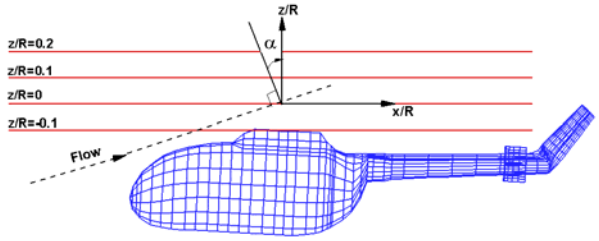

Figure 3 Panelization of the Bo105 fuselage, tail boom and empennage. Red lines indicate the position of the planes of data extraction

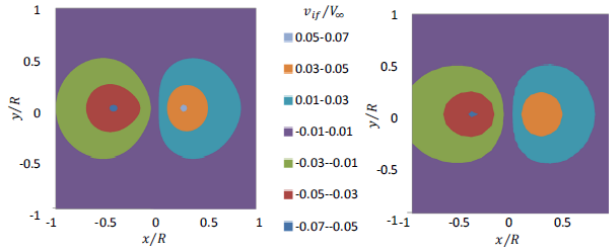

(a) UPM data, (b) analytical model

Figure 4 induced inflow ratio normal to the rotor rotational plane above the hub center for Isolated fuselage, α=0°

Based on the fuselage-induced velocity distributions computed by CFD or UPM for the isolated fuselage and extracted in four planes parallel to the rotor rotational plane as shown in Figure 3, the parameters (A_0, S_{x0}, S_{y0}) of the analytical mathematical formulation of the induced velocity v_i can be identified such that the math model allows a reconstruction of the fuselage-induced velocity field with small errors within the

entire data volume defined by the four planes. A best fit to the pre-computed flow field was obtained using a multi-variable optimizer, based on the sum of squared errors to be minimized[13].

Since the formula are asymptotically approaching zero for large values of x, y and z, the model can be used even outside this volume. In the application, the fuselage effect on the rotating blades as well as on the wakes of the MR can be computed analytically instead of the full UPM modelling of the fuselage, which spares a significant amount of CPU time. An example of the quality of this model is shown in Figure 4 comparing the data of the UPM with those of the analytical model. A downwash velocity is defined as positive in Figure 4.

In this paper, the model uses the pre-computed flow field around the isolated BO105 fuselage using UPM. The separation of the flow which can occur from the hub or hub fuselage area is not simulated. The fuselage consists of 1152 panels.

2.1.4 Modeling of free wake generation

The free wake is represented in the form of connected vortex filaments. The model of free wake consists of following steps:

a) At the start of the computation there are no wakes present.

b) With each time step, all rotor blades or wings move to a new position with a velocity which is relative to the ground fixed frame of reference and consists of translation, rotation and other motion. Figure 2 shows the wake strip comprising a series of quadrilateral ring vortices after having been released from the downstream edge of the Kutta panel. The spanwise variation of the circulation on this new row of wake panels is the same as that on the Kutta panels and will keep unchanged throughout the whole computations.

c) After each computation step, a new wake strip is created and added to the previous wake. The whole wake surfaces are then freely deformed according to the locally induced velocity.

d) With the generation of the wake its induction effect is included to satisfy the flow tangency condition for the next computation step.

A full-span free wake is generated in this manner step by step behind the blades or wings as the computation proceeds. The free wake analysis requires no initial condition.

As the computation time sharply increases with increasing length of the wake, the length of wakes can be fixed to save the computational time [15]. This is true for steady flight since the general shape of freely developed wake remains almost unchanged after several revolutions. When the length of the wake reaches the user defined limit, the filaments at the end of the wake are cut off.

In the MR/TR/Fuselage case, in general, the computation of MR and TR should be started simultaneously. The rotors are simply started impulsively from rest and the free wakes are generated step by step with the developing rotor motion. Usable results could only be obtained after initial wakes pass away from both rotors. In order to save CPU-time, it is helpful to start running MR/Fuselage computation independently at first for several revolutions until the MR initial wakes pass through TR rotational plan and then switch on the TR computation and run MR/TR/Fuselage simultaneously.

2.2 CFD Code FLOWer

FLOWer is a structured multi-block computational fluid dynamics (CFD) code and has been developed at DLR [11]. As it has been successfully coupled with HOST in [14], FLOWer is used to cross-check the results obtained by the UPM coupling, as well as to see the difference occurring from the different aerodynamic solutions. Here, FLOWer is used with the classical 2nd order Jameson scheme in space with low dissipative settings (k_2=0.5, k_4=96) and matrix dissipation and a 2nd order dual-time stepping scheme based on an explicit Runge-Kutta scheme with implicit residual smoothing. The multi-grid technique is used to accelerate convergence. On the one hand, the inviscid Euler formulations are solved, which should yield similar aerodynamic results as UPM with the addition of compressible effects, while on the other hand the viscous Navier-Stokes equations are solved using the k-ω SST turbulence model. The grid generation is done by an in-house tool based on the transfinite interpolation as presented in [14]. In all cases a four-bladed Chimera computation setup is used, with the background mesh having about half the total grid points spent, and the each blade mesh about one eighth each. For the Euler computations, three mesh sizes are investigated, the total setups consist of 1 million, 8 million, and 61 million grid cells, while the Navier-Stokes setup features 15 million points and is similar to the 8 million grid with the exception of an added boundary layer resolution.

During the coupling process, only the blade lift is exchanged for the inviscid computations to be consisted with UPM results, while the Navier-Stokes solutions couples lift, drag and the pitching moment of each section with HOST.

2.3 DLR's comprehensive rotor code S4

DLR's high resolution 4th generation rotor simulation code (S4) has its origins in the mid-'70s with rigid flapping, constant downwash, and steady table look-up of aerodynamic coefficients. Today, S4 is used for analysis of any kind of active rotor control with respect to performance, dynamics, and noise and for support of wind tunnel testing[2][15].

The structural dynamics modeling consists of two parts. First, a finite element method (FEM) acts as off-line pre-processor and performs the modal analysis, i.e., it computes the coupled mode shapes and natural frequencies in vacuo. The major component of the modes is used to compute all modal forces and moments related to the blade mass prior to the simulation. Major inertial couplings are taken into account here. In a second step, the rotor simulation itself solves the dynamic response problem of these modes (which are reduced to their major component) subjected to the aerodynamic loading in the form of a modal synthesis.

For two-dimensional unsteady compressible section airloads, a semi-empirical analytic formulation of the airfoil coefficients $C_n M^2$, $C_m M^2$, and $C_t M^2$ is used within S4. Furthermore, a distinction between unsteady aerodynamics due to body motion (causing a constant or linear variation of velocities along the airfoil chord) and due to gusts (as caused by a vortex with strong non-linearity along the chord) is made. The tip loss of lift is accounted for in the outer 5% of the blade by modifying the induced velocities progressively towards the tip such that the zero lift angle of attack is obtained there. Also, fuselage interference flow is computed at the blade sections by an analytical formulation derived from potential theory calculations [16]. Within this study, the Bo105 fuselage was taken into account which recently was modeled and included in S4 [17], based on UPM panel method data. The methodology is outlined in detail in [12].

2.4 Airbus Helicopters comprehensive rotor code HOST

The comprehensive code HOST[10] is developed by Airbus Helicopters France (formerly Eurocopter France) and is applied in a wide range of applications. HOST itself features simplified aerodynamics based on the blade element theory, which relies on 2D look-up tables. On the structural side, the extended version of the Bernoulli beam theory is solved assuming small deformations in lead-lag, flap and torsion. An offset between the elastic and neutral axes from the center of gravity is accounted for in HOST; however, shear and elongation of the blade are neglected. To finally solve the aero-mechanic problem, the Lagrange equations are formulated at each blade segment, which is connected with the others segments by real or virtual joints. To be computationally more efficient a modal approach is used within HOST, which reduces the degrees of freedom and decouples time and space. A Newton-Raphson based trim-procedure drives the system state towards user-defined trim objectives. In addition, HOST always uses the rigid body mode with equivalent hinges for the first mode. Only higher modes are formulated elastically by beam theory.

2.5 Coupling

A weak coupling method between the HOST or S4 dynamic codes and the free wake panel code UPM for computing the trim of a flexible rotor is applied. During the coupling, the UPM provides the corrections to the simplified aerodynamics (currently only lift) embedded in either S4 and HOST, while on the other hand, the blade deformation in time (azimuth) and space (radial direction) provided by HOST or S4 are taken into account into panel coordinates. A trim procedure was applied in order to reach the experimental thrust coefficient and hub moments (pitch and roll).

The coupling procedure itself is based on the delta aero loads approach. It is described in more detail in [10].

The delta airloads approach gradually replaces the 2D aerodynamics of the comprehensive codes with 3D aerodynamics until the global loads purely consist of 3D loads. The aerodynamic forces at each coupling step are given by:

$$F^n_{HOST/S4}(\Psi) = F^{n-1}_{3D}(\Psi) + \Delta F^n_{2D}(\Psi)$$

The superscript n denotes the n-th coupling cycle. During the second coupling cycle, the section loads are taken from the previous 3D simulation and only the change, $\Delta F^n_{2D}(\Psi) = F^n_{2D}(\Psi) - F^{n-1}_{2D}(\Psi)$ due to varying blade deflections are calculated based on the 2D.

This coupling procedure is repeated until it converges to $F_{HOST/S4}(\Psi) = F_{3D}(\Psi)$ and the blade deflection does not change between the coupling steps.

2.6 Trim computation

For the isolated MR cases, the trim itself is established by driving the system towards a set state. Here the flow conditions such as rotor shaft, advance ratio and RPM are fixed, while the pitch

control angles θ_0, θ_C and θ_S are determined by the trim algorithm of S4 or HOST to reach the set lift, roll and pitching moment of the rotor hub.

In MR/TR/Fuselage interaction cases, the trim consists of two steps. In the first step, the MR/Fuselage is trimmed by the trim algorithm of S4 or HOST. In the second step, the TR is added in the computation starting from the trimmed MR/Fuselage condition and the trim for the TR is started. The trimmed MR/Fuselage control angle from first step is applied to the MR, assuming effect of the TR on the MR/Fuselage trim can be neglected. For the TR trim, an internal force trim procedure is applied in UPM. The force trimming procedure applied in the numerical simulation adjusts the pitch **θ** in such a way that the thrust, the pitch and roll moment of the TR matches the experimental values. For the see-saw motioned BO105 TR, the pitch [**θ**] - flap [**β**] (teeter) angle coupling has been taken into account. UPM internal trim procedure is applied for the rigid blade computations.

2.7 The Aeroacoustic Model

The Aeroacoustic Prediction System based on an Integral Method, APSIM has been developed at the DLR Institute of Aerodynamics and Flow Techniques for prediction of rotor or propeller noise radiated in the free far-field. The method is designed to calculate wave propagation over large distances in uniform flows and has been extended recently to couple with CFD and CAA methods for propagating any noise signal to the far field. The methodology is based on the Ffowcs-Williams/Hawkings (FW-H) formulation [18] for porous and blade surfaces and only linear sound propagation is taken into account. In general the aeroacoustic computation into the far field is split into two steps: In a first step the aerodynamic flow field or the pressure data on the body is computed by an aerodynamic code and provided to APSIM; in a second step the sound propagation into the far field is calculated with APSIM.

3. RESULTS FOR VALIDATION ON COUPLING PROCEDURE FOR ISOLATED MAIN ROTOR

In order to verify that the coupling algorithm works correctly and to illustrate the effects of elastic blade motion on the aerodynamic and noise footprints, the simulation results are compared with available wind tunnel results. The validation is done with a 6° descent flight condition in which BVI is dominant source of aerodynamic unsteadiness and noise.

Table 1 Main Rotor (MR) data

Property	MR
no. of blades	4
rotor type	hingeless
radius	2 m
radius scale factor	2.455
chord	0.121 m
root cut-out	0.44 m
solidity	0.077
precone	2.5°
pretwist	-8°/R
pitch-flap coupling	0°
tip Mach number (ISA)	0.64
lock number	8
shaft tilt forward	3°
shaft tilt upward	0°
airfoil	NACA 23012

The investigated flight conditions are listed in the following table and belong to two wind tunnel campaigns, HART2 and HeliNoVi. In both test cases, the wind speed and the rotor shaft angle are prescribed, while the shaft angle of the experiment was corrected for the wind tunnel interference according to the open jet test section and the rotor thrust. This correction was computed using the Heyson method.

Both the HART II and the Helinovi rotor are a 40% Mach and dynamically scaled model of Bo105 hingeless rotor, operated at 1041 RPM. Technical data of the main rotor is listed in Table 1. The flight condition and trim data are given in Table 2.

Table 2 Trim conditions for the validation

Speed	Main Rotor					
V_∞ m/s	M_h	$10^4 \cdot C_T$	M_x NM	M_y NM	α_{eff} deg	Test
33	0.64	45.7	20	-20	4.5	HART 2
33	0.64	50.4	-14.	179	3.6	Helinovi

The computations of UPM are started with a step equivalent size of 5° MR azimuth and this is reduced to 1° after initial wakes pass away from the rotor. The MR blade is discretized by 46 panels along the airfoil contour and 9 panels along the span with totally 414 panels for each blade.

3.1 Case 1; HART 2 baseline, 6° descent flight at 33m/s (coupling with S4)

The coupling of S4 and UPM is conducted for this flight condition. The comparison of the control angle is given in Table 3. The comparison indicates that due to the effect of the elastic torsion, the coupled computation requires more collective pitch (θ_0),

which is in contrast to the rigid blade simulation. The rigid blade results fit better with the test. In comparison with the rigid blade simulation, the trim procedure requires less the lateral control (θ_C) and longitudinal cyclic (θ_S) control angle in elastic case. The difference of longitudinal cyclic from test is generally smaller.

Table 3 MR control angle

MR Control Angle(°)	θ_0	θ_C	θ_S
Test	3.8	1.92	-1.34
rigidMR(UPM)	3.72	2.06	-1.33
MR(S4+UPM)	4.01	1.57	-1.20

3.1.1 Deformations

The blade deformation examined here are the elastic blade twist or torsion and flapping. The blade tip motion is defined here as the pure elastic deflection time history relative to parameters like the pre-cone in flap direction and the pre-twist of the blade as well as the blade pitch control angles. The predicted elastic twist and flap at the blade tip is compared in Figure 5. The measured data which is shown as blue line with symbols were obtained from blade 1 using the Stereo Pattern recognition (SPR) technique.

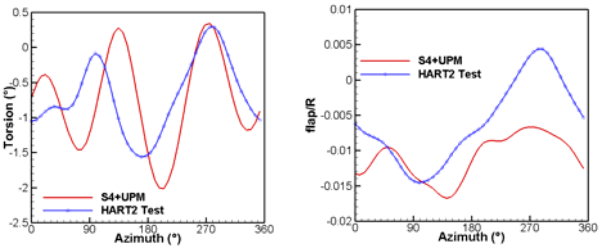

Figure 5 comparison blade tip elastic torsion motion relative to control and pre-twist (right) and tip elastic flapping motion relative to precone (right)

In both cases, prediction and test, the torsion (Figure 5 left) at blade tip are quite similar to each other on blade retreating side, and a 3-per-rev elastic torsion is observed in the simulation, while the test (blue line) mainly has a 2/rev content. There is some offset in phase on advancing side at minimum torsion position. There is stronger flap-torsion coupling imbedded in dynamic modeling in S4 than in HOST.

A 1/rev variation is seen in the tip flap motion with maximum occurring at about 280◦ azimuth for both simulation and test as shown in Figure 5 on the right. There is phase shift in the minimum deflection.

In addition, a positive rolling moment (right side down) in the trim is represented by higher flap position at 280° in both test and simulation.

3.1.2 Airloads

The $C_N M^2$ results at r/R=0.87 are compared in Figure 6. The measured data (averaged over several MR revolutions) is represented as blue solid line with diamonds, while the continuous red and green lines denote the predicted results from elastic (coupled) and rigid blade simulations, respectively. Zero TR azimuth angle (Azimuth=0°) is defined as blade position when the blade points downstream. In general a predominant 2/rev load is observed in both test and rigid blade simulation, while there is 3/rev in elastic blade simulation, which is caused by the 3-per-rev elastic torsion.

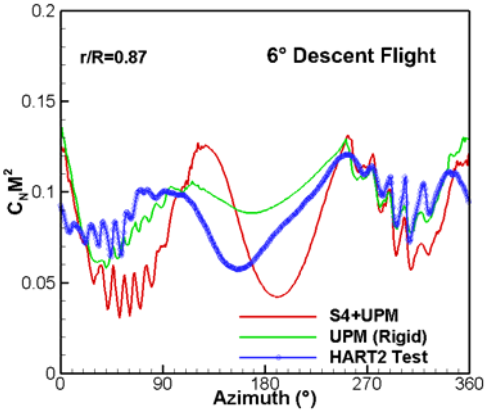

Figure 6 MR normal force coefficient at 0.87R for 6° descent fligth

The high frequency fluctuations in both the experimental and simulated sectional load in both 1st and 4th quadrant clearly indicate the presence of strong BVI phenomena which makes the MR the dominating factor of the total noise radiation during this flight condition. There is an underestimation on the unsteadiness in these two BVI quadrants in the rigid blade simulation, especially on the advancing blade side. There is only a minor improvement in terms of BVI amplitude on retreating blade side for the elastic computation.

3.1.3 Acoustics

To gain insight into the directivity of the generated noise under the influence of the elastic blade deformation, Figure 7 compares the noise contour plot at mid-frequency summary level (6thBPF-40BPF) between rigid simulation (left), elastic

simulation (middle) and wind tunnel measurements (right). The location of the MR disc is indicated by the black circle. Two maximum noise areas (hot spots) are captured, one on the advancing and one on retreating side in the predicted noise contour. The influence of the elastic motion generally improves the prediction of the hot spots both in directivity and amplitude.

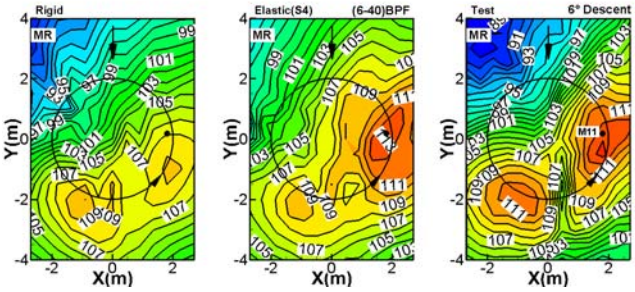

Figure 7 Simulated and measured (right) BVI noise contours

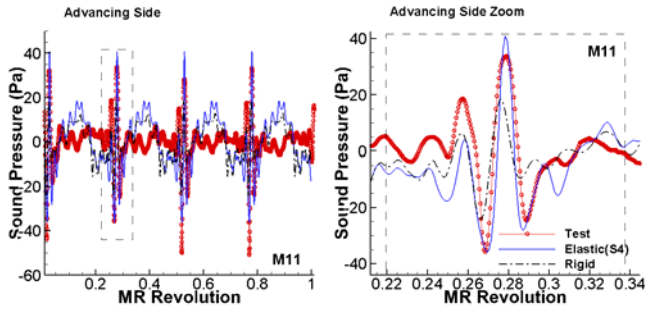

Figure 8 Acoustic pressure time histories taken from M11, as shown in Figure 7

Figure 8 compares the acoustic pressure time histories taken from a microphone position (M11) located on the advancing side, as shown in Figure 7. The zoomed part of the time history indicates a typical advancing side BVI signal starting from under pressure and followed by sharp over pressure. The time histories show good agreement in both phase and amplitude for the main BVI peak with the experiment when coupling with a dynamic code.

3.2 Case 2; Helinovi, 6° descent flight at 33m/s (coupling with HOST)

The coupling of HOST and UPM is analyzed for the descent flight condition. Additionally, the FLOWer/ HOST coupling is also sketched in the plots for comparison with CFD. The fuselage is not yet included in the any of the simulations in this section.

The control angle from the trim procedure is given in Table 4. In comparing with rigid blade simulation, the effect of the elastic deformation requires less lateral control (θ_C) and longitudinal cyclic (θ_S), but more collective pitch (θ_0) as consequence of the negative torsion in the simulation. This result is similar as S4/UPM coupling for the HART 2 case.

Table 4 MR control angle at 6° descent flight

MR Control Angle(°)	θ_0	θ_C	θ_S
Test	4.5	1.8	-0.6
rigidMR (UPM)	5.04	1.85	-1.21
MR(HOST+UPM)	5.21	1.82	-0.84
MR(HOST+Flower) inviscid	4.46	1.47	-0.56
MR(HOST+FLOWer) viscous	4.7	1.48	-0.39

3.2.1 Deformations

The predicted elastic twist and flap is plotted at two blade sections in Figure 9. There was no direct measurement of these two variables in the experiments, therefore the comparison with S4/UPM as well as HOST/Flower coupling results is presented and in addition, measured torsion and flap moment which reflect the behavior of blade deformation are also given for comparison in Figure 10 and Figure 11, respectively. For HOST/CFD(Flower) coupling, three mesh sizes for the inviscid simulation are investigated as well as one mesh size for the viscous approach. The results given here are from finest mesh size of the inviscid computation.

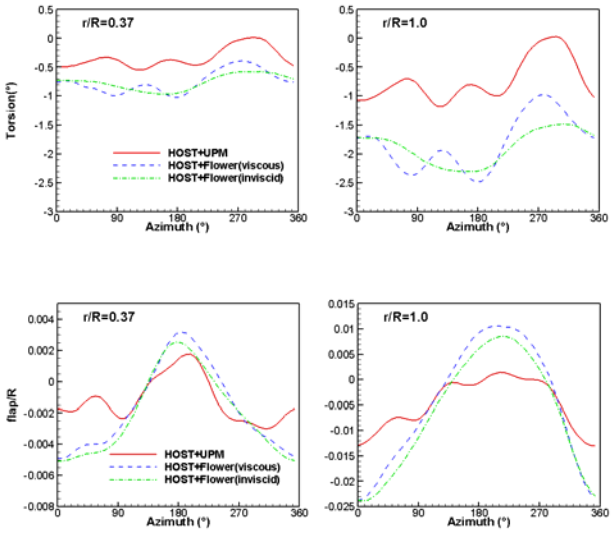

Figure 9 comparison blade elastic torsion motion relative to control and pre-twist (top) and elastic flapping motion relative to precone (bottom)

The prediction of the torsion (Figure 9 top) at two radial sections shows a weaker 3-per-rev elastic torsion. The maximum torsion angle in the HOST/UPM simulation (Figure 9 top) at about 280° on retreating blade side is met with the measured torsion moment presented in Figure 10.

Interestingly, this 3-per-rev behavior is not observed for the inviscid FLOWer based computation, but for the viscous HOST/Flower, instead of only C_L coupling, the coupling of C_L, C_D and C_m. Opposing to the UPM results, both FLOWer simulations have a stronger blade torsion, which is attributed to the influence of compressibility. Compressibility leads to stronger forces towards the blade tip and thus stronger deflections. While the 3-per-rev oscillation seems to be an over-prediction when compared to Figure 10, the overall shape of the deformation curves correlate with the curves of the measured torsional moments.

A 2/rev variation is seen with maximum upward position at about 190◦ azimuth for HOST/UPM as shown in Figure 9 bottom for the flap deformation, while only a 1/rev variation is seen for the HOST/Flower coupling.

The higher flap position at 190◦ azimuth than in the back at 0° is in accordance with the trim situation of a positive pitching moment (nose up). This behavior is in accordance with measured blade flap moment in Figure 11, in which the maximum occurs at 180°.

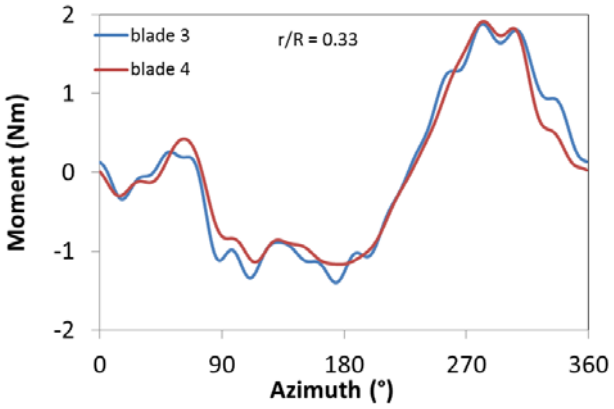

Figure 10 the measured torsion moment at one radial section of two blades, representing blade torsion (mean value removed)

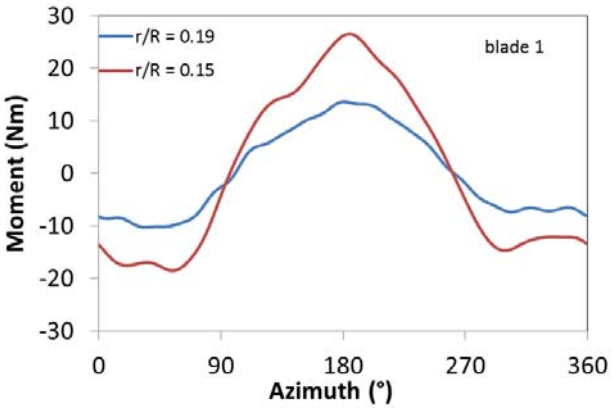

Figure 11 the measured flap moment at two radial sections, representing blade flap (mean value removed)

3.2.2 Airloads

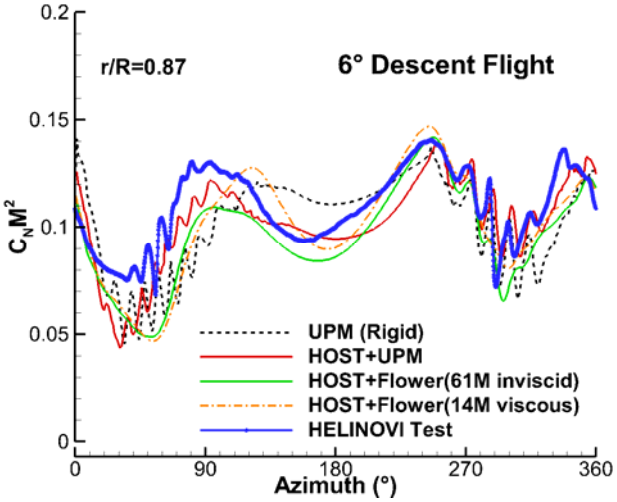

Figure 12 MR normal force coefficient at 0.87R for 6° descent flight

The $C_N M^2$ results at r/R=0.87 are illustrated in Figure 12. The measured data is represented as a blue solid line with diamonds, while the continuous red and green lines denote the inviscid predicted results with the elastic blade model coupled with either UPM or Flower. The result for the rigid blade is given by the black dashed line, and the orange line denotes the viscous results by FLOWer. In general a predominant 2/rev load is observed for the experimental and computed data.

Similar to the HART 2 case in previous section, the high frequency fluctuations in sectional load in the 1st and 4th quadrant clearly indicate the presence of strong BVI phenomena. This is captured well by UPM, however FLOWer only shows a minor

resolution of BVI on the retreating side in the form small wiggles for the 61M Euler mesh. The coarse mesh only manages to show the averaged value of the loads (Results not shown here). Overall, it is seen that the prediction is improved by including the elastic deformations in the computation.

3.2.3 Acoustics

Figure 13 depicts the mid-frequency summary level (6thBPF-40BPF) noise contour plots of rigid (left) and elastic (middle) simulations along with the measurements (right).The two predictions align well with the experimental results. Similar to the HART II case, two BVI hot spots exist for this descent case. The peak magnitudes of the BVI signals are slightly reduced under the influence of the elastic motion, yet the agreement is still fairly good relative to the wind tunnel results.

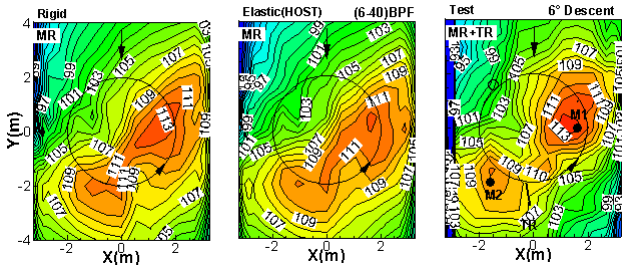

Figure 13 Simulated and measured (right) BVI noise contours

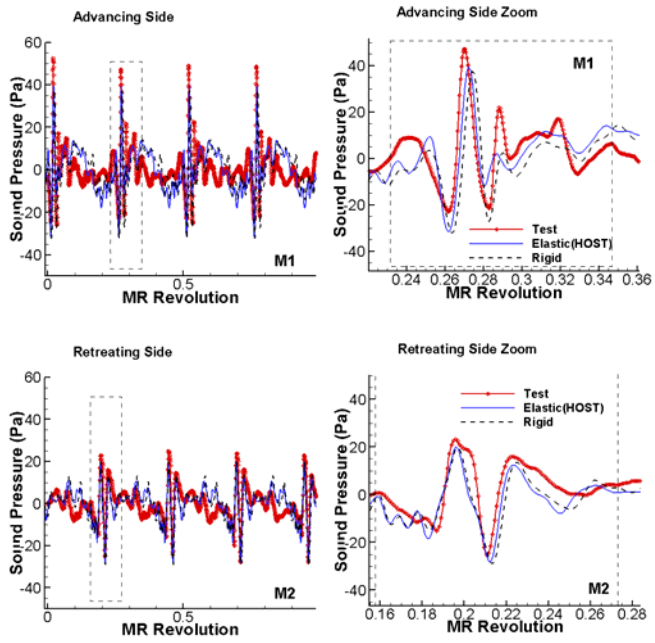

Figure 14 Acoustic pressure time histories taken from M1 and M2, as indicated in Figure 13

Figure 14 shows the acoustic pressure time histories taken from 2 microphone positions (M1, M2), marked on the right of Figure 13. The peak phase and amplitude are well matched by the both simulations in accordance with the experiments.

4. MAIN ROTOR RESULTS UNDER THE INFLUENCE OF ELASTIC BLADE DEFORMATION AND DIFFERENT FUSELAGE MODELING

The effects of the fuselage on the mutual interference as well as noise characteristics are investigated for several HELINOVI cases as shown in Table 5. The coupling of HOST and UPM is always conducted for all flight condition.

Table 5 Trim conditions for MR

	Flight Cond.		Main Rotor				
ID #	V_∞ (m/s)	θ_{FP} (deg)	M_h	$10^4 \cdot C_T$	M_x (NM)	M_y (NM)	α_{eff} (deg)
1	33	12	0.641	52.9	-101	189	-14.6
2	60	0	0.641	52.0	-66	236	-6.8
5	33	-6	0.641	50.4	-14	179	3.6

In terms of the fuselage modelling, both potential theory in form of a panelised fuselage and the analytic fuselage influence formulation are investigated.

4.1 Case 1; Helinovi , 6° descent flight at 33m/s

The effect of fuselage modeling is small for this flight conditions when comparing the control angles of the simulations in Table 6.

The effect on the overall lift is negligible, which is seen from the invariant collective pitch (θ_0) for all simulations. The lateral control angle (θ_C) is slightly increased under influence of the fuselage, which then also reduces the flapping of the blade at azimuth 180° as shown in Figure 15, thus the change in tip path plane angle is small. The change of the longitudinal cyclic (θ_S) due to the presence of the fuselage is relatively small, which is decided by the shape of the fuselage. In addition, the trend of the changing of the blade control angles is very similar for both forms of the fuselage modeling.

Table 6 MR control angle at 6° descent flight

MR Control Angle(°)	θ_0	θ_C	θ_S
Test	4.5	1.8	-0.6
MR(No FUS)	5.21	1.82	-0.84
MR (+FUS)	5.22	1.97	-0.93
MR(+FUSForm)	5.21	1.99	-0.90

FUS=FUSelage, FUSForm=analytic FUSelage Formulation

4.1.1 Deformations

The blade torsion is shown in Figure 15 (top) at two radial sections for the three configurations. 1- and 3-per-rev elastic torsion is seen with the maximum torsion occurring at about 290° on retreating blade side for all configurations. The overall deviation is less than 0.2° between the various fuselage representations.

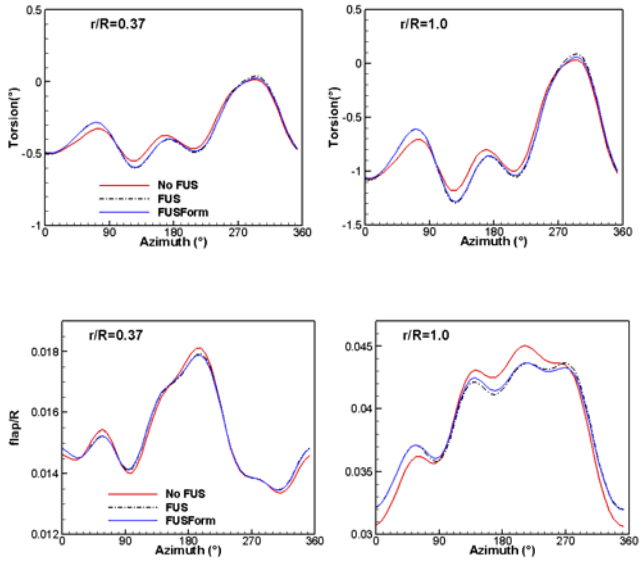

Figure 15 comparison blade elastic torsion motion relative to control and pre-twist (top) and elastic flapping motion (precone included) (bottom)

A 1/rev and 2/rev flap variation with the maximum peak at about 190◦ azimuth remains for the fuselage models as shown in Figure 15 (bottom).

4.1.2 Airloads

The MR normal force coefficient $C_N M^2$ at 87% radial station is given Figure 16 for one MR revolution for different configurations. The inclusion of the fuselage improves slightly the correlation against the measured data in the 1st and 2nd quadrant of MR revolution. The predictions of the different fuselage models track each other pretty closely.

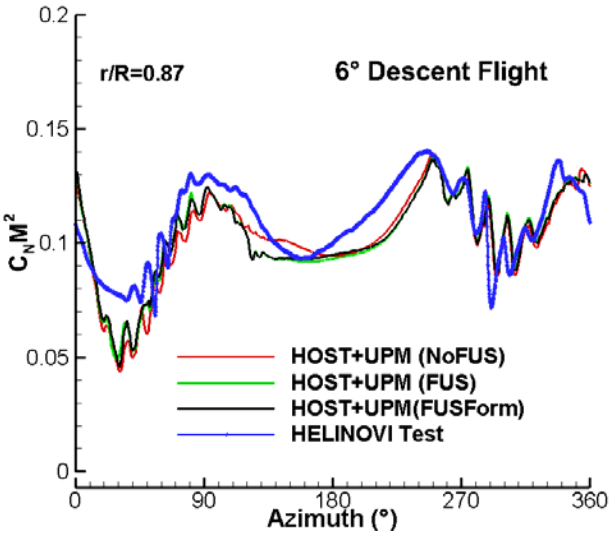

Figure 16 MR Normal force coefficient at 0.87R for 6° descent flight

4.1.3 Acoustics

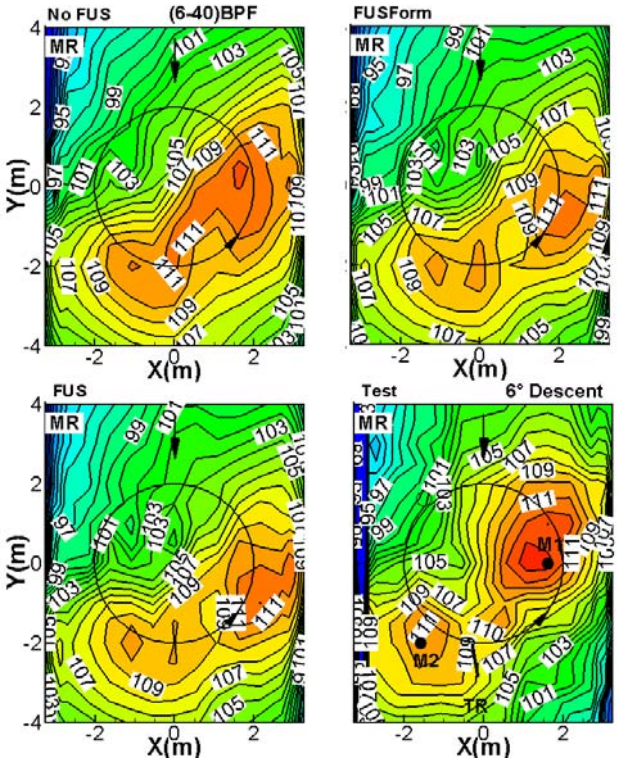

Figure 17 Simulated and measured (right) BVI noise contours for various fuselage modelings

Figure 17 compares the noise contour plots for mid-frequency summary level (6thBPF-40BPF) of the simulations with measurement (bottom right). The influence of the fuselage reduced the maximum MR BVI noise in both advancing and retreating side by

1dB. The contour plot for the two fuselage models bears strong similarity.

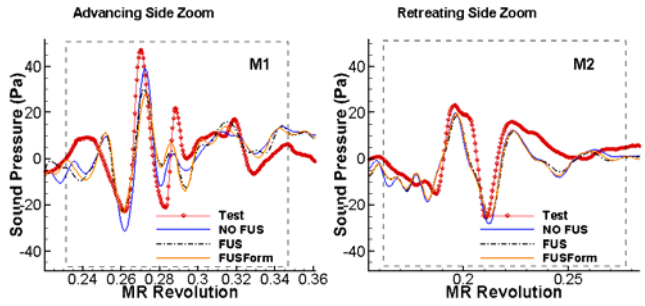

Figure 18 Acoustic pressure time histories taken from M1 and M2, as indicated in Figure 17

Figure 18 shows the comparisons of the acoustic pressure time histories taken from 2 microphone positions (M1, M2), as shown in Figure 17 right bottom. The presence of the fuselage reduces BVI noise on the advancing side, where M1 is located.

By looking at the tip vortex in an advancing side BVI position at about ψ =40° azimuth angle of the reference blade as shown in Figure 19, there is a slightly larger miss distance of the tip vortex to the blade in the rotor-fuselage case. This is due to the effect of the upwash of the fuselage to slow down the rotor downwash and the convection of the tip vortex towards the blade is reduced in rotor-fuselage case, which increases slightly the miss distance of the tip vortex to the blade. Therefore a reduction of BVI is expected in rotor-fuselage.

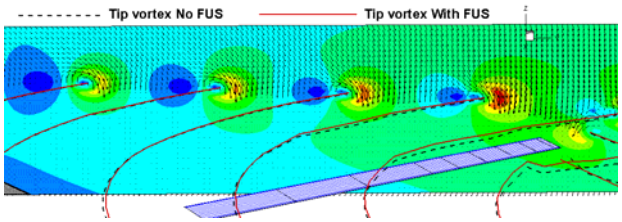

Figure 19 Enlarged closer view of the tip vortex in the advancing side BVI position at 40° azimuth

4.2 Case 2; Helinovi , 12° climb flight at 33m/s

Similar to the descent, the effect of the fuselage on the collective pitch (θ_0) is negligible among three configurations, see Table 7. Under the influence of the fuselage, the lateral control (θ_C) is slightly increased in comparison with the non-fuselage case. The increment of the lateral control (θ_C) is compensated by the reduction of blade flapping at azimuth 180° as shown in Figure 20 (flap). The change of the longitudinal cyclic (θ_S) due to the presence of the fuselage is relative small. Again, the trends of the control angles are very similar for the two forms of fuselage modeling.

Table 7 MR control angle at 12° climb flight

MR Control Angle(°)	θ_0	θ_C	θ_S
Test	9.0	1.7	-1.6
MR(NoFUS)	9.67	1.84	-1.47
MR (+FUS)	9.67	1.99	-1.59
MR(+FUSForm)	9.66	2.04	-1.53

4.2.1 Deformations

The blade torsion and flap are shown in Figure 20 at two blade sections for the three configurations. 1-per-rev variation occurs for both torsion and flap. Similar to descent flight, the maximum torsion occurring at about 290° in retreating blade side, while the maximum flap is located about 120° azimuth angle. In general, the effect of the fuselage on blade deformation is small.

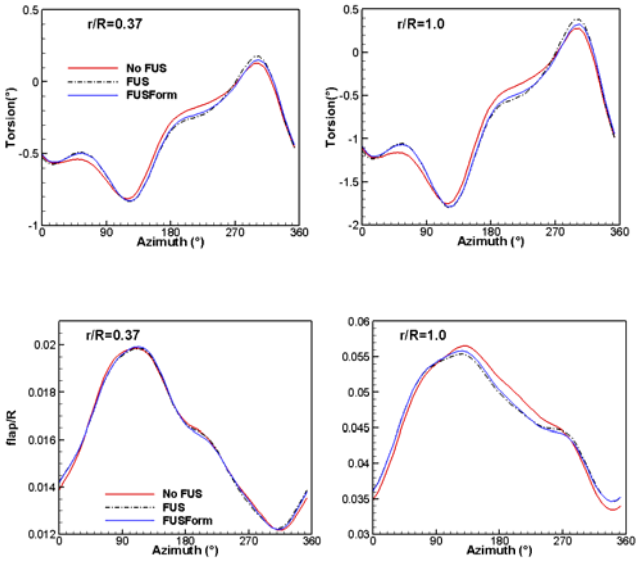

Figure 20 comparison blade elastic torsion motion relative to control and pre-twist (top) and elastic flapping motion (precone included) (bottom)

4.2.2 Airloads

The MR Normal force coefficient at 87% radial station is plotted in Figure 21 for the 12° climb flight case. Both the averaged experimental and simulation results are shown in Figure 21. They indicate a low-frequency 2/rev oscillation behavior of

$C_N M^2$ throughout the revolution with a drop occurring around 90° on the advancing side and 280° on the retreating side. This low frequency 2/rev oscillation in $C_N M^2$ will contribute to the low frequency noise, especially at even number of BPF. In addition, there is small unsteadiness about 90° for all simulated configurations, but this small unsteadiness is not seen in the experiment. Presumably, the lack of viscosity leads to a stronger vortex modelling, leading to BVI on the advancing side. However, the unsteadiness on the advancing side is still questionable, and further studies are necessary to confirm this.

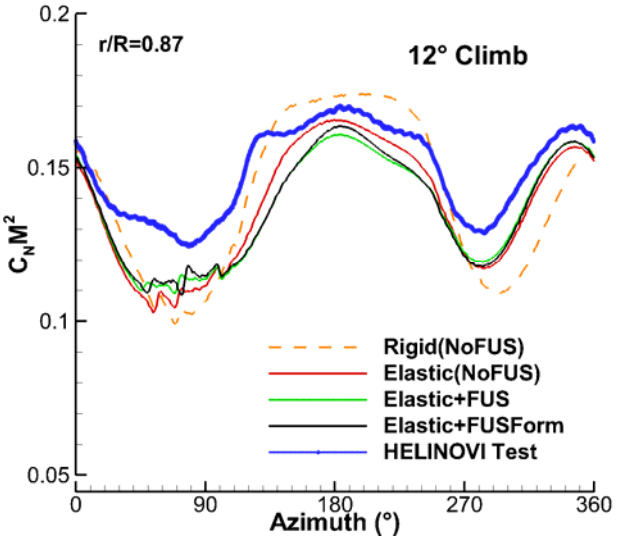

Figure 21 Normal force coefficient at 0.87R for 12° climb flight

The simulations capture the experimental trend well; yet, a slight offset exists over the whole revolution. The plateau before and after 180° is not resolved by the elastic computations. In terms of the influence of the elastic deformation on blade loading, the overall improvement in complete revolution is observed.

4.2.3 Acoustics

Considering the characteristics of the low frequency contents in the normal force coefficient, which contribute to the low frequency noise, the noise contour plot of the overall sound pressure level (OSPL) is used to compare the simulation with the test results, as shown in Figure 22. As the noise contour plot for two fuselage model bear strong similarity, only the result for the panelised fuselage model is plotted.

The position of the maximum noise level upstream of the MR (typical low frequency loading noise) is captured for all configurations as seen in the plots. The inclusion of the fuselage in the simulation reduces difference from the test in terms of peak value.

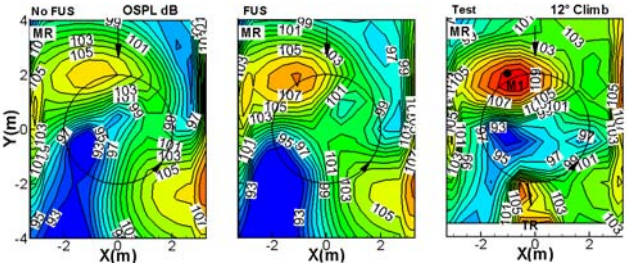

Figure 22 Simulated and measured (right) OSPL noise contours for various fuselage modeling

The noticeable hot spot downstream of the MR in the experiment result is believed to be the low frequency background noise due to interaction of microphone and vortices shed from support system. This type of noise is not simulated.

Figure 23 gives the comparisons of the acoustic pressure time histories taken from the microphone positions M1. The time histories indicate that inclusion of the fuselage improves the correlation of the peak value.

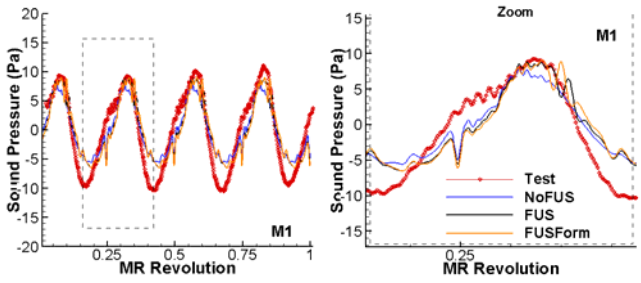

Figure 23 Acoustic pressure time histories taken from M1, as indicated in Figure 22

4.3 Case 3; Helinovi , level flight at 60m/s

The effect of the fuselage on the control angle for the rotor trim is similar to the other flight condition with the final values listed in in Table 8.

Table 8 MR control angle at level at 60m/s

MR Control Angle(°)	θ_0	θ_C	θ_S
Test	8.3	0.8	-3.3
MR(NoFUS)	8.93	1.15	-3.23
MR (+FUS)	9.01	1.38	-3.47
MR(+FUSForm)	8.97	1.41	-3.37

4.3.1 Deformations

The characteristics of the blade torsion and flap, shown in Figure 24, are quite similar in terms of variation from the climb condition, except for the flap at blade tip where a strong 2-per-rev with two maxima, one at 90° and one at 270° are identified.

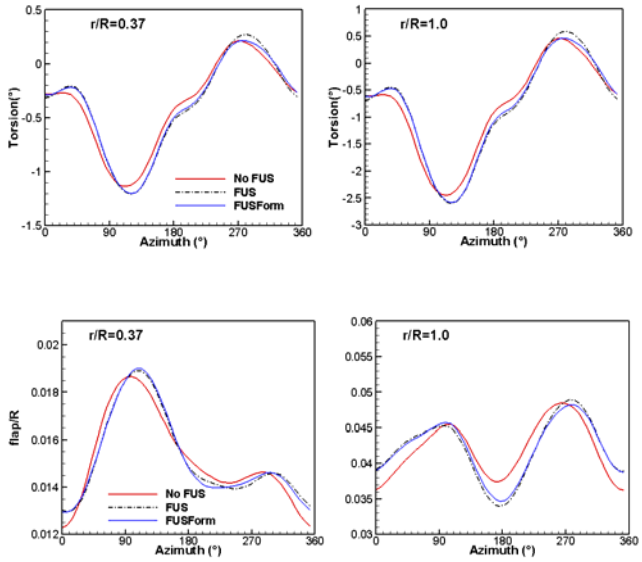

Figure 24 comparison blade elastic torsion motion relative to control and pre-twist (top) and elastic flapping motion (precone included) (bottom)

4.3.2 Airloads

For the level flight (Figure 25) a $C_N M^2$ "drop" on advancing blade side in the experiment is shifted to 130° in comparison with the climb flight. This phenomenon is likely to be determined by the co-existence of strong compressibility, aeroelastic and interactional effects. By increasing the complexity in the simulation starting from rigid blade to the elastic blade with fuselage, each improvement bring the simulation results closer to the test results, although there is still a phase shift of the "drop" between the test and the simulation. The trend of the local minimum at 270° is correctly predicted despite differences in value and location of the $C_N M^2$ global minimum. Despite the simplicity of the analytical fuselage model (FUSForm), the overall effects are correctly predicted.

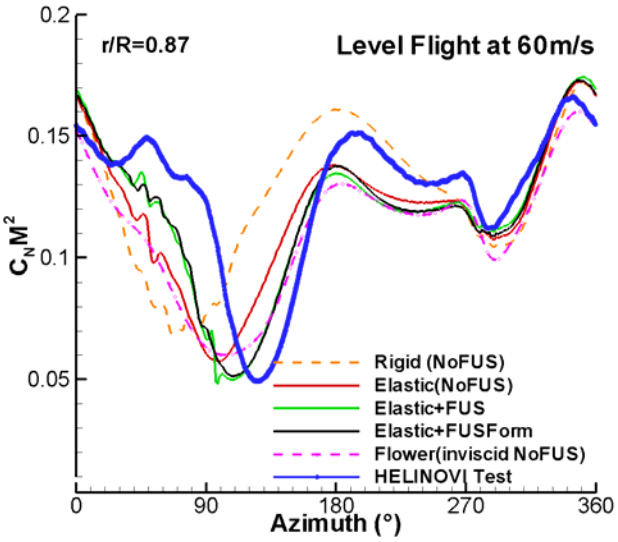

Figure 25 Normal force coefficient at 0.87R

Similar to the climb condition, there also exists a small unsteadiness in 1st quadrant of the simulation, which does not show up in the experiment. The unsteadiness located around 90° disappears when using the analytical fuselage formulation in the simulation. It is likely that the analytical formulation leads to a different convection of the wake, which increases the miss distance. The reason for this unsteadiness in the simulations still needs for further studies.

The comparison with the result of the HOST/Flower coupling indicates again the importance of the elasticity in predicting the 'drop' in the advancing side for this flight condition. Although a simplified compressibility correction (Prandtl-Glauert) is used in UPM, the comparison with CFD still shows a relative good agreement.

4.3.3 Acoustics

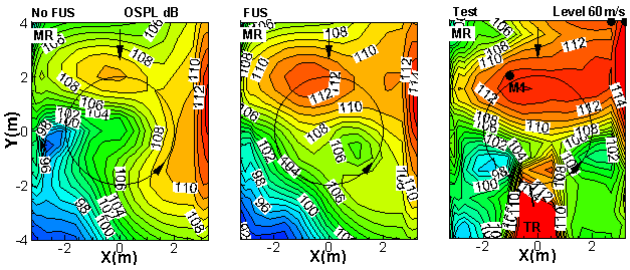

Figure 26 Simulated and measured (right) OSPL noise contours for various fuselage modeling

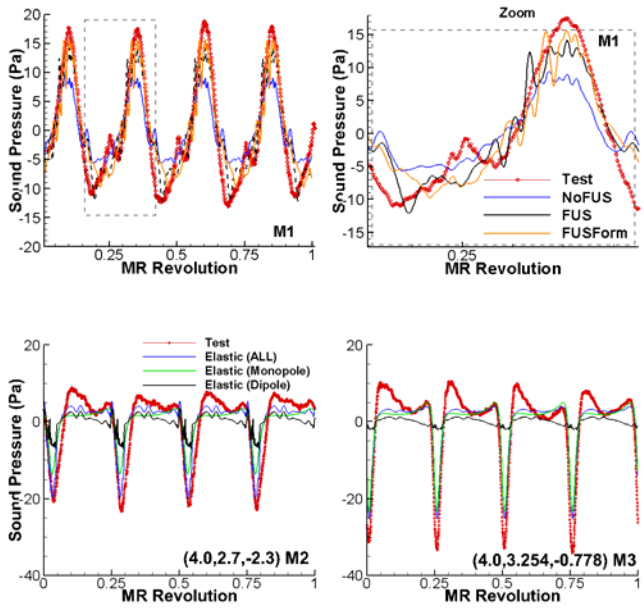

Figure 27 Acoustic pressure time histories taken from M1, as indicated in Figure 26

The overall sound pressure level contour plots are given in Figure 26 where similar to the climb case, only the panelised fuselage model results are shown as the two fuselage models only differ little.

Similar to the climb flight, the position of the maximum level upstream of MR is captured for all configurations. When comparing with the climb condition as shown in Figure 22, the upstream noise becomes louder, which is attributed to the increase of the forward flight speed. This trend is also captured by the simulation with the fuselage included one being better. However, there is still a good offset to the experiment, which is attributed to the lack of compressibility effects in UPM as well as the lack of quadruple noise in the simulation.

The increased background noise of the support strut (hot spot located downstream of the MR) as shown in Figure 26 (right) is again due to the increased wind speed. As indicated before, this type noise is not simulated.

Figure 27 shows the comparisons of the acoustic pressure time histories taken from 3 microphone positions (M1, M2, M3).The time history for M1 indicates that the inclusion of the fuselage improves the correlation of the noise peak value as a consequence of improving the correlation of the blade loading. M2 and M3 are located upstream around the tip rotational plane where thickness and quadruple noise play an important role. The difference between the simulation and the test at peak region, especially for M3 indicates the contribution of the quadruple noise coming from shock waves, which is neglected in the noise simulation.

5. TAIL ROTOR RESULTS UNDER INFLUENCE OF MAIN ROTOR AND FUSELAGE

A BO105 MR/TR/Fuselage configuration, as shown in Figure 1 is used. The TR is trimmed as specified in section 0. Technical data of the tail rotor are listed in Table 9.

Table 9 Technical data of the tail rotor

Property	TR
no. of blades	2
rotor type	teetering
radius	0,383 m
radius scale factor	2.48
chord	0.074 m
root cut-out	0.16 m
solidity	0.123
precone	0°
pretwist	0°/R
pitch-flap coupling	45°
tip Mach number (ISA)	0.61
lock number	4.2
shaft tilt forward	-4°
shaft tilt upward	-3°
airfoil	S102E

The tail rotor was run at a slightly slower speed (approx. 6% slower) for the scaled model than the real BO105. The objective of this is to provide an integer ratio between main and tail rotor speeds in order to facilitate numerical simulations. In this case 5 tail rotor revolutions match one main rotor revolution and results in a tail rotor tip Mach number of 0.614. It is not believed that this change has any impact on the character of the interaction between main and tail rotors.

Table 10 Trim conditions for TR

	Flight Cond.		Tail Rotor				
ID #	V_∞ (m/s)	θ_{FP} (deg)	$M_{\Omega R}$	$10^4 \cdot C_T$	M_x (NM)	M_y (NM)	
1	33	12	0.614	90.9	0.0	0.0	climb
2	60	0	0.614	54.5	0.0	0.0	level

In MR/TR/Fuselage interaction cases, only the TR is trimmed, while the trimmed MR or MR/Fuselage control angle as well as blade deformations are taken from the previous test and applied to the MR, assuming that the effect of the TR on the MR or the MR/Fuselage trim can be neglected. An internal force trim procedure is applied to trim the TR to the given value as listed in Table 10. Only two flight conditions, 12° climb and high speed level flight are considered here, in which the TR is major source of noise.

The computations started with a step size of 5° MR azimuth and this was reduced to 1° after initial wakes pass away from both rotors. This corresponds to a rotation of 5° of the TR. Each TR blade consists of 210 panels.

5.1 Case 2; Helinovi , 12° climb at 33m/s (ID1)

The comparison of the TR control angles for various configurations is listed in Table 11. The control angles applied for the MR in the simulation are given in Table 7. In general, the influence of the MR alone or MR+Fuselage requires less TR collective pitch (θ_0) in comparison with the test value. In contrast to the isolated TR, the influence of MR alone or MR+Fuselage on both the TR collective pitch (θ_0) and the longitudinal cyclic (θ_S) is about 1°. In comparison with MR+TR, the influence of the fuselage on the TR control angle is less than 0.1°. The effect of the fuselage or elastic MR on the TR collective pitch (θ_0) is about 0.05° and is negligible.

Table 11 TR control angle at 12° Climb

TR Control Angle(°)	θ_0	θ_C	θ_S
Test	6.50	-1.90	1.60
Isolated TR	7.56	-1.75	0.48
+rigidMR	6.16	-2.76	0.83
+elasticMR	6.20	-2.84	0.84
+elasticMR+FUS	6.15	-2.86	0.86

5.1.1 Airloads

The Effect of the MR+TR or MR+TR+Fuselage interaction on TR $C_N M^2$ can be demonstrated more clearly by comparing with isolated TR case in one TR revolution, as shown in Figure 28 for 12° climb case at two radial stations r/R=0.8, 0.97. Two test results (one averaged over several TR revolutions, marked as AVG and one taken from instant time history, marked as single) are given in the plot for comparison. Zero TR azimuth angle is defined when the blade points downstream.

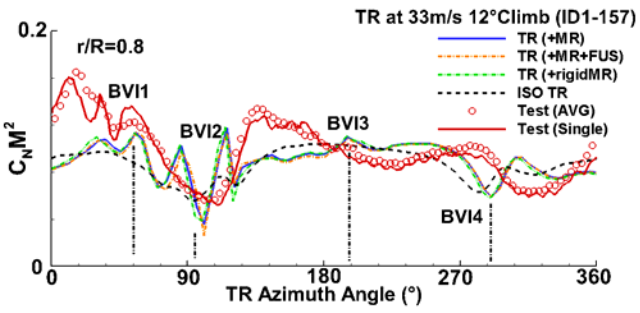

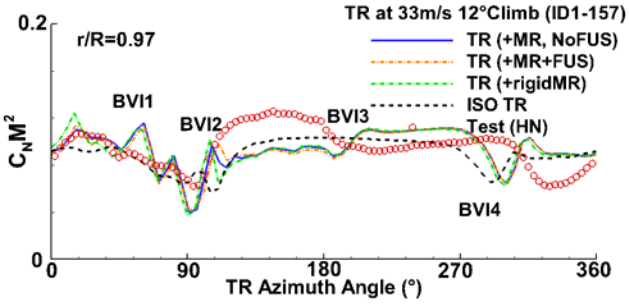

Figure 28 TR normal force coefficient at 0.8R and 0.97R for 12° climb flight

In general all the configurations except isolated TR resemble similar characteristics in terms of the peaks or valleys in the $C_N M^2$ time history for two given sections, which indicates that the effect of the fuselage or the elasticity of the MR on the TR is relative small for this flight condition. The comparison indicates that BVI like peaks marked as BVI 1 and 4 show up in both the simulation and the test. The strong BVI 2 is only observed in the simulation. It has to be mentioned that the averaged value of the experiment data is relative smooth in comparison with the single time history. Due to the possible deviation of MR and TR rotational speeds from their nominal values as well as the not completely synchronized MR-TR driving system in the experiment, the averaging can smooth the BVI peaks in the test results.

In order to clarify the real cause of these peaks in the simulation, several snap shots of the TR tip vortex under MR/TR configuration (solid line) and isolated configuration (dashed line) are given in Figure 29 for various TR azimuth positions where the behavior of BVI 1, 2, and 4 are located. For a better clarity, only the tip vortex which is main interaction with TR is sketched.

In general, under the induction of the MR wake, the TR tip vortex trajectory deforms considerably in comparison with the isolated TR case (dashed line) and the wake deformation causes the tip vortex moving closer to TR rotational plane, so that the miss distance between the blade and the wake is reduced and therefore stronger BVI occurs. Figure 29 indicates that cause of BVI 1, 2, 4 is mainly due to the TR interacting with its own tip vortex (self-BVI). BVI 1 (Figure 29a) is introduced by the TR blade interacting with tip vortex trailed by the proceeding blade, while BVI 2 (Figure 29b) only shown up in the simulation is generated due to interaction with its own tip vortex. BVI 4 causes a drop in $C_N M^2$ at about 270° due to the interaction of the TR blade with the tip vortex trailed by the preceding blade as shown in Figure 29c.

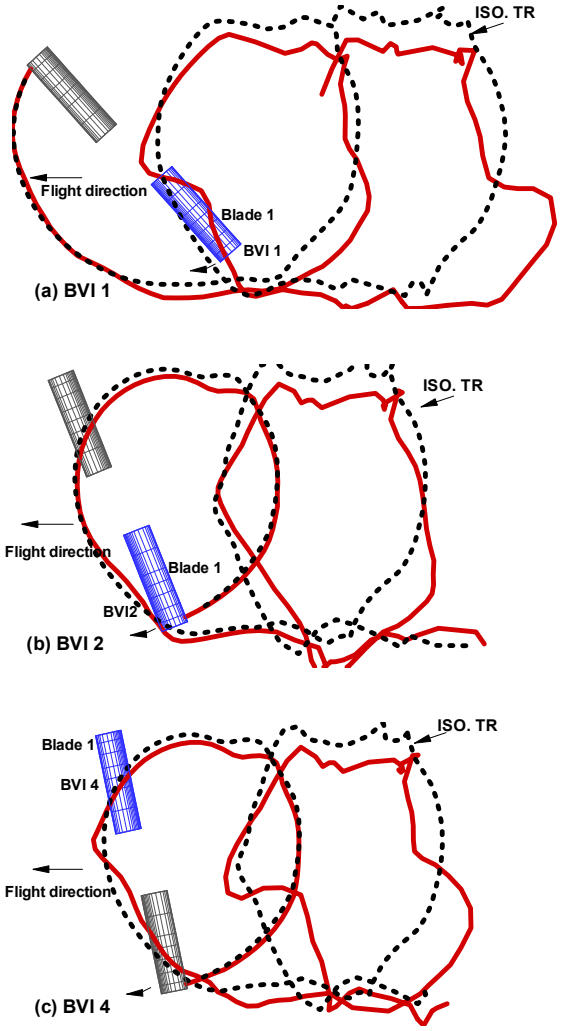

Figure 29 Snap shots of the TR tip vortex under MR/TR (solid line) and isolated configurations (dashed line) for various TR azimuth positions where TR self-BVI occurred

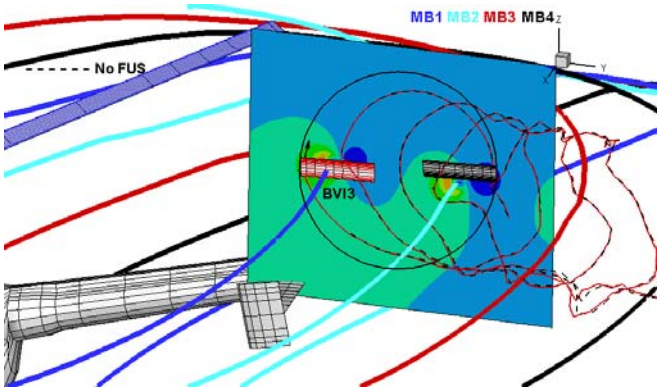

Figure 30 Perspective view of MR and TR wakes at TR azimuth position about 195° where TR perpendicular interaction with MR tip vortex occurs

Figure 30 gives a perspective view of MR and TR tip vortexes at TR azimuth position about 195° where BVI3 occurred as shown in Figure 28. The relative position among TR, MR, MR tip vortexes and MR wakes (not shown in plot for clearness) indicate that the localized $C_N M^2$ variations around 195° is mainly caused by both the TR blade-MR tip vortex and TR blade-MR wake interactions as well as interaction between TR blade and MR potential field which become sharper for the section closer to the tip.

5.1.2 Acoustics

The full scale dBA as shown in Figure 31 was evaluated for a full configuration including MR(elastic)+TR+Fuselage. The choice of full scale dBA as the metric was dedicated by the necessity to highlight the TR BVI content of the spectrum. The location of the MR disc and TR rotation plane are indicated by the circle and thick line respectively. The results show that the contribution of the TR noise as shown in Figure 31 on the upper left indicate two noisy regions located in both TR thrust- and outflow-direction with major contribution of TR loading noise, while the contribution of the MR noise is directed on upstream of MR and is 5dBA less noisy. Therefore in this flight condition, the TR noise is the dominant source of the noise.

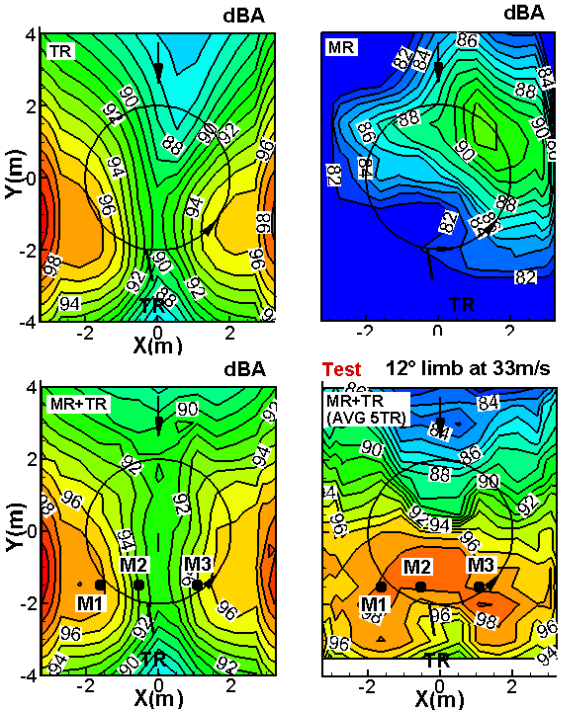

Figure 31 Comparison of full scale dBA contours with test for the contribution of the TR, the MR and the MR+TR under the configuration of MR+TR+FUS

The characteristics of the noise distribution also shows up in the test result (Figure 31 lower right) with a general agreement in noise level as simulation on both the TR thrust- and outflow-side, but with a slightly offset in position. An additional noisy area occurs just upstream of the TR and around the TR rotational plane in the test results doesn't show up in the simulations.

The comparison of the noise contour plot for different configurations, such as TR+MR(rigid), TR+MR(elastic) and TR+MR(elastic)+Fuselage is given in Figure 32. Only the contribution of the TR noise is compared for the clarity. In general, the directivity from TR for all three configurations looks very similar and indicates two distinct noisy regions located on both TR thrust- and outflow-direction. A slight increase of this noisy region is observed under the influence of the fuselage.

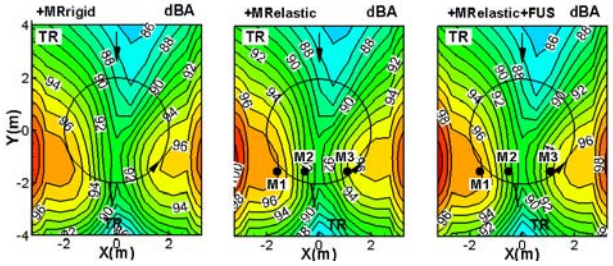

Figure 32 Simulated and measured full scale dBA TR noise contours at three different configurations

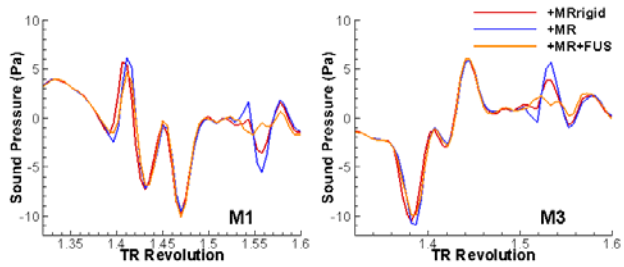

Figure 33 TR acoustic pressure time histories taken from 2 microphone positions as shown in Figure 32 for different configurations

Figure 33 gives the comparisons of the acoustic pressure time histories taken from 2 microphone positions, as shown in Figure 32, where the tail rotor loading noise is expected to be more pronounced. Only one blade passing period is shown for a better forcus.

5.2 Case 2; Helinovi , Level flight at 60m/s (ID1)

The comparison of the TR control angles for various configurations is listed in Table 12. The control angles applied for the MR in the simulation is given in Table 8. The characteristics of the control development as a function of different configurations are similar to the climb flight. The differences of the rigid, the elasticity or the fuselage have the tendency of reducing collective pitch (θ_0), while the influence on the longitudinal cyclic (θ_S) and the lateral control (θ_C) is relatively small.

Table 12 TR control angle at level flight

TR Control Angle(°)	θ_0	θ_C	θ_S
Test	5.00	-0.40	2.40
Isolated TR	5.33	-1.83	1.32
+rigidMR	4.46	-1.94	1.57
+elasticMR	4.31	-1.91	1.52
+elasticMR+FUS	4.15	-2.01	1.57

5.2.1 Airloads

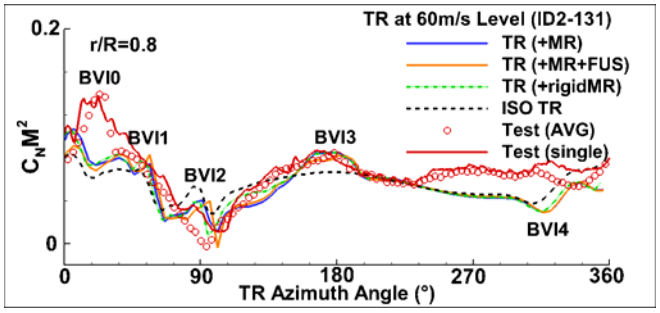

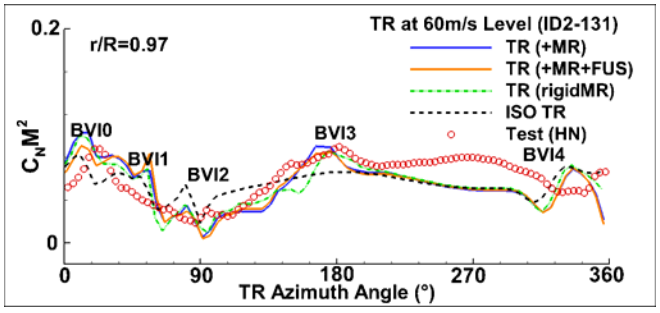

Figure 34 TR normal force coefficient at 0.8R and 0.97R for level flight

Figure 34 shows the comparison of $C_N M^2$ in one TR revolution for ID2 60m/s level flight case at radial stations r/R=0.8, 0.97 for different configurations. The comparisons with 12° climb case indicate similar self-BVI behavior occurring on the advancing side for BVI1 and BVI2 as well as on the retreating side for BVI 4, but with less intensity in amplitude. Although the BVI2 is hardly seen in averaged test data (open circle), it shows up in non-averaged time history (red line). There is a peak marked as BVI0 which occurred in the test and the simulation around the TR azimuth position where the TR blade 1 points

downstream. This is the location where the TR blade tends to interact with the MR tip vortex.

5.2.2 Acoustics

Figure 35 shows the comparison of the simulated and measured full scale dBA contours for a full configuration including MR(elastic)+TR+Fuselage at 60m/s level flight. The simulated contribution of TR and MR noise for the MR+TR-Fuselage configuration indicate that the TR is the major source of noise in 60m/s level flight in the region of TR thrust- and outflow-direction, while the MR noise also plays an important role on the MR advancing side. In comparison with the 12° climb case, increasing MR and TR noise levels are observed which can be due to increasing local tip Mach number. The comparison with the test results shows that the general characteristics in terms of both noise directivity and the maximum noise level are captured. The remaining differences are attributed to the lack of compressibility modelling (the quadruple noise).

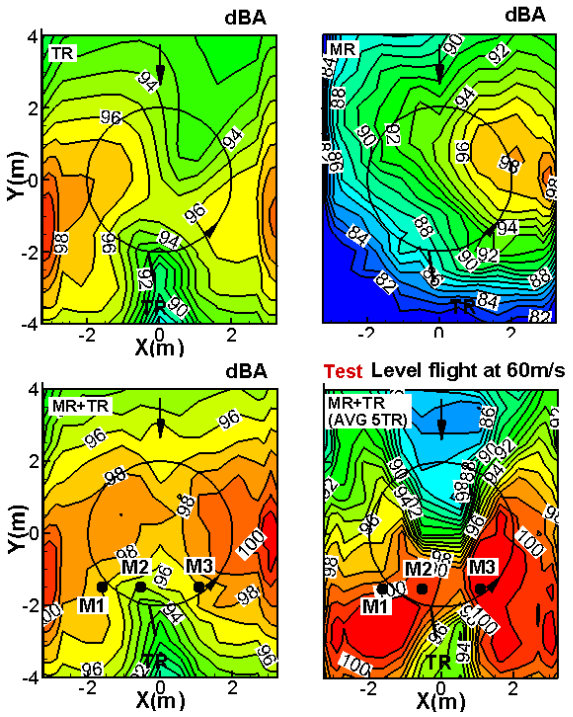

Figure 35 Comparison of full scale dBA contours with test for the contribution of the TR, the MR and the MR+TR under the configuration of MR+TR+FUS

Figure 36 compares the noise contour plots for different configurations, such as TR+MR(rigid), TR+MR(elastic) and TR+MR(elastic)+Fuselage. The influence of the MR elasticity causes a reduction of the maximum noise in the TR thrust-direction. In general, the changing of the directivity is hardly seen.

Figure 37 gives the comparisons of the acoustic pressure time histories taken from 2 microphone positions, as shown in Figure 36 indicate the difference among the configuration.

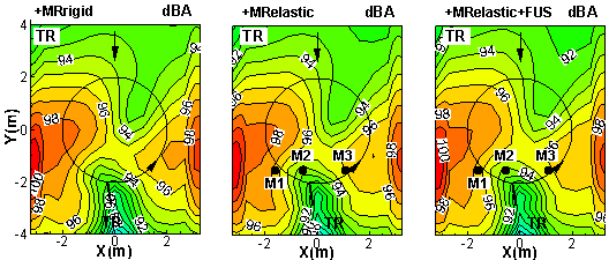

Figure 36 Simulated full scale dBA TR noise contours at three different configurations

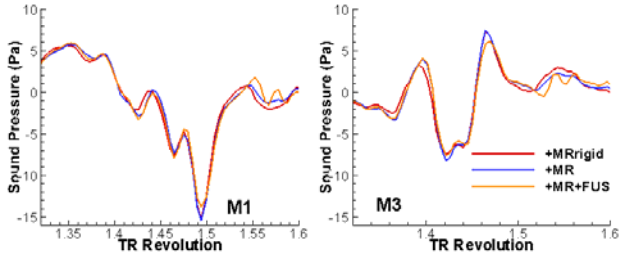

Figure 37 TR acoustic pressure time histories taken from 2 microphone positions as shown in Figure 36 for different configurations

CONCLUDING REMARKS

An unsteady free wake panel code coupled with the comprehensive rotor codes was used to account for the effect of the elastic blade deformation and the fuselage on the rotor aerodynamic and radiated noise. The effect of the fuselage was simulated by using two different fuselage models. The sound propagation into the far field was calculated with a FW-H code. The influence of both the MR elastic deformation and the fuselage on the MR and TR aerodynamic and the noise at three different flight conditions were presented and compared with test results and CFD simulations.

In general, the inclusion of the MR elastic blade deformation in the aerodynamic simulation has clearly improved the correlation against the measured data for all three computed flight conditions.

1. 6° descent flight where the MR is the major source of noise

The comparison of the control angles indicated that the coupled computation require more collective pitch as an effect of the elastic torsion and the trim procedure requires less lateral control and longitudinal cyclic control angle in the elastic case.

The effect of fuselage modeling is small for this flight condition and the effect on the overall lift is negligible. The change of the longitudinal cyclic pitch due to the presence of the fuselage is relatively small, which is determined by the shape of the fuselage.

The influence of the elastic motion has in general improved both directivity and amplitude of the noise in both advancing and retreating side. The influence of the fuselage reduced the maximum MR BVI noise in both advancing and retreating side. The influence of fuselage has in general caused a reduction of maximum MR BVI in both advancing and retreating side as the effect of the upwash of the fuselage is to slow down the rotor downwash and the convection of the tip vortex towards the blade is reduced in the rotor-fuselage case, which increases slightly the miss distance of the tip vortex to the blade. The azimuth positions of BVI were hardly changed under the influence of the fuselage.

2. Low speed climb and high speed level flight where the TR is the major source of noise

For the MR, increasing the complexity in the simulation starting from rigid blade to the elastic blade with fuselage, each improvement bring the simulation results closer to the test results. The effect of the fuselage on the collective pitch is negligible, but the influence of the fuselage on the lateral control is slightly increased in comparison with the non-fuselage case. The position of the maximum noise level upstream of the MR (typical low frequency loading noise) is captured for all configurations. The inclusion of the fuselage in the simulation reduces the difference from the test in terms of the peak value.

For the high speed level flight, in comparison with CFD results, the compressibility effect in the simulation is good captured by the simplified Prandtl-Glauert compressibility correction used in UPM.

For the TR, the influence of the MR alone or MR+Fuselage on the TR control angle is similar in both flight conditions. The MR has a big impact on the TR. The effect of the fuselage increases slightly the TR BVI at advancing side, when the TR blade passes over the vertical stabilizer and therefore causes an increase of the TR BVI noise.

The comparison between the experimental results and the numerical ones highlighted once more the extreme complexity of the aerodynamic phenomena involved in a complete helicopter configuration operating at different flight conditions.

REFERENCES

[1] M. Smith, J. Lim, B. van der Wall, J. Baeder, R. Biedron, D. Boyd Jr., B. Jayaraman, S. Jung, B-Y. Min, “The HART II international workshop: an assessment of the state of the art in CFD/CSD prediction”, CEAS Aeronautical Journal, 4 (4), pp. 345-372, 2013.

[2] B.G. van der Wall, J.W. Lim, M.J. Smith, S.N. Jung, J. Bailly, J.D. Baeder, D.D. Boyd, Jr. “An Assessment of Comprehensive Code Prediction State-of-the-Art Us-ing the HART II International Workshop Data”. CEAS Aeronautical Journal, 4 (3), pp. 223-252, 2013.

[3] J. Yin “Prediction - and its Validation - of the Acoustics of Multiblade Rotors in Forward Flight Utilising Pressure Data from a 3-D Free Wake Unsteady Panel Method”. Proceedings, 20th European Rotorcraft Forum, 04. - 07.10.94 in Amsterdam/Niederlande.

[4] S.R. Ahmed, V.T. Vidjaja, “Unsteady Panel Method Calculation of Pressure Distribution on BO105 Model Rotor Blades“, Journal of the American Helicopter Society, pp. 47-56, Jan. 1998.

[5] J. Yin, S.R. Ahmed, “Helicopter main-rotor/tail-rotor interaction”. Journal of the American Helicopter Society, Vol. 45 (No. 4), pp. 293 -302, 2000.

[6] J. Yin “Main Rotor and Tail Rotor Blade Vortex Interaction Noise under the Influence of the fuselage”, 38th European Rotorcraft Forum, Amsterdam, The Netherlands, Sept. 4-7, 2012.

[7] H.-J. Langer, O. Dieterich, S. Oerlemans, O. Schneider, B.G. van der Wall, J. Yin “The EU HeliNOVI Project - Wind Tunnel Investigations for Noise and Vibration Reduction”, 31st European Rotorcraft Forum, Florence, Italy, Sept. 13-15, 2005.

[8] J. Yin, B.G. van der Wall, S. Oerlemans “Representative Test results from HELINOVI Aeroacoustic Main Rotor/Tail Rotor/Fuselage Test in DNW”; 31st European Rotorcraft Forum; Florence, Italy; Sept. 13-15, 2005.

[9] J. Yin, B.G. van der Wall and S. Oerlemans, “Acoustic wind tunnel tests on helicopter tail rotor noise (HeliNOVI)”, Journal of the American Helicopter Society , 53 (3) , Seiten 226-239.

[10] B. Benoit, A.-M. Dequin, K. Kampa, W. von Grünhagen, P.-M. Basset, B. Gimonet “HOST, a General Helicopter Simulation Tool for Germany and France”, AHS 56th Annual Forum and Technology Display, Virginia Beach, VA, May 2-4, 2000.

[11] J. Raddatz and J. Fassbender, "Block structured Navier–Stokes solver FLOWer, in: MEGAFLOW – Numerical Flow Simulation for Aircraft Design," Numerical Fluid Mechanics and Multidisciplinary Design, vol. 89, no. 1, pp. 27-44, 2005.

[12] B.G. van der Wall, A. Bauknecht, S.N. Jung, Y.-H. You “Fuselage-Rotor Mutual Interference: a Step towards Interactional Aerodynamics in Comprehensive Codes”; 5th Decennial Aeromechanics Specialists Conference, Fisherman’s Wharf, San Francisco, CA, Jan. 22-24, 2014.

[13] van der Wall, B.G., Bauknecht, A., Jung, S.N., You, Y.H.: Semi-Empirical Modeling of Fuselage-Rotor Interference for Comprehensive Codes: The Fundamental Model, CEAS Aeronautical Journal, DOI:10.1007/s13272-014-0113-4, May 2014

[14] "Aeroelastic Simulations of Isolated Rotors Using Weak Fluid-Structure Coupling," in High Performance Computing in Science and Engineering ’06, Berlin Heidelberg, Springer

[15] B.G. an der Wall, Analytic Formulation of Unsteady Profile Aerodynamics and its Application to Simulation of Rotors, ESA-TT-1244, 1992 (Translation of the Research Report DLR-FB 90-28, 1990)

[16] B.G van der Wall, C. Göpel,“Über den Einfluss der Rotorversuchsstände ROTEST und ROTOS auf die Rotordurchströmung im DNW“. (About the Influence of the Rotor Test Rigs ROTEST and ROTOS on the Flow in the Rotor Disk in DNW), DLR-Mitteilung 91-16, 1991

[17] B.G van der Wall, A. Bauknecht, S.N. Jung,Y.H. You, “Semi-Empirical Physics-Based Modeling of Fuselage-Rotor and Fuselage-Wake Interferences for Comprehensive Codes”. 70th Annual Forum of the American Helicopter Society, Montréal, Canada, May 20-22, 2014.

[18] J.E. Ffowcs Williams and D.L. Hawkings, “Sound Generation by Turbulence and Surfaces in Arbitrary Motion”, Philosophical Transactions of the Royal Society, A264, pp. 321-342, 1969.

COPYRIGHT STATEMENT